

Cite this: *Nanoscale*, 2017, **9**, 13313

Ultrafast structural dynamics of boron nitride nanotubes studied using transmitted electrons†

Zhongwen Li,[‡] Shuaishuai Sun,^{‡,a,b} Zi-An Li,^a Ming Zhang,^{a,b} Gaolong Cao,^a Huanfang Tian,^a Huaixin Yang^{a,b} and Jianqi Li^{*a,b,c}

We investigate the ultrafast structural dynamics of multi-walled boron nitride nanotubes (BNNTs) upon femtosecond optical excitation using ultrafast electron diffraction in a transmission electron microscope. Analysis of the time-resolved (100) and (002) diffraction profiles reveals highly anisotropic lattice dynamics of BNNTs, which can be attributed to the distinct nature of the chemical bonds in the tubular structure. Moreover, the changes in (002) diffraction positions and intensities suggest that the lattice response of BNNTs to the femtosecond laser excitation involves a fast and a slow lattice dynamic process. The fast process with a time constant of about 8 picoseconds can be understood to be a result of electron–phonon coupling, while the slow process with a time constant of about 100 to 300 picoseconds depending on pump laser fluence is tentatively associated with an Auger recombination effect. In addition, we discuss the power–law relationship of a three-photon absorption process in the BNNT nanoscale system.

Received 11th June 2017,
Accepted 4th August 2017

DOI: 10.1039/c7nr04162d

rs.c.li/nanoscale

Introduction

Owing to their novel physical properties that differ from those of their bulk counterparts, intense research studies on one-dimensional (1D) tubular nanomaterials have led to many new concepts and applications.^{1,2} One prominent example is carbon nanotubes (CNTs)³ that exhibit rich transport properties including insulating, semiconducting and metallic behaviors depending on their tubular chirality.⁴ Structurally similar to CNTs, boron nitride nanotubes (BNNTs)⁵ also have tubular structures but only exhibit semiconducting transport with a large band gap regardless of their tubular chirality.⁶ Although the BNNTs are not explored for their conduction channels in nanoscale electronic devices due to their insulating transport properties, recent studies^{7–9} have demonstrated novel applications including BNNT-based tunnel field-effect transistors (TFETs) with suppressed leakage current and low contact resistance. The exploitation of nanoscale electronic devices based on these tubular nanostructures requires a full understanding of not only their static structural characteristics

but also their structural response to externally applied stimuli, *e.g.*, thermal heat and electromagnetic waves.¹ In this regard, the fast development of new instrumentation and novel approaches that can provide an access to ultrafast structural dynamics of nanostructured materials is highly appreciated.

In recent years, rapid progress has been made in the use of the ultrafast pump–probe approach based on transmitted electrons in a transmission electron microscope.¹⁰ Several groups^{10–14} worldwide have demonstrated the development of ultrafast transmission electron microscopy (UTEM) and its applications to ultrafast structural dynamics of solids. One great advantage of employing transmitted electrons in a UTEM for time-resolved studies is the strong matter–electron interactions to yield reliable signals related to fast dynamics processes.¹⁵ This is of particular importance for the dynamical studies of nanostructured materials with inherently small volume or mass. UTEM studies of the structural dynamics of CNTs have revealed intriguing ultrafast changes in the electronic structure¹⁶ and lattice relaxation.^{17,18} A second advantage of ultrafast dynamics studies on a UTEM lies in the fact that a UTEM can be operated both for ultrafast dynamics and static structural characterization by switching between pulse-laser-excited and thermionic electron sources. For this purpose, we successfully modified a conventional JEM-2000EX microscope into a UTEM that allows us to study not only the ultrafast structural dynamics of materials in both diffraction and imaging, but also their conventional static structures, as demonstrated in our previous publications.^{18,19}

Here, we investigate the structural dynamics of BNNTs by means of ultrafast electron diffraction experiments using our

^aBeijing National Laboratory for Condensed Matter Physics, Institute of Physics, Chinese Academy of Sciences, Beijing 100190, China. E-mail: lj@aphy.iphy.ac.cn

^bSchool of Physical Sciences, University of Chinese Academy of Sciences, Beijing 100049, China

^cCollaborative Innovation Center of Quantum Matter, Beijing 100084, China

†Electronic supplementary information (ESI) available: The fitting of a mono-exponential function to the experimental (002) peak, the temporal evolution of interlayer space along the radial direction with pump fluence of 25 and 50 mJ cm⁻², and the EELS measurement of BNNTs. See DOI: 10.1039/c7nr04162d

‡These authors contributed equally to this work.

UTEM. We characterize the lattice response of the highly anisotropic tubular structure of BNNTs upon laser excitation and assess the characteristic time constants for the electron-phonon coupling and other lattice dynamics processes. The obtained characteristics of structural dynamics in BNNTs are compared with those of the analogous tubular structure of CNTs and those of their bulk counterpart hexagonal BN.

Experimental

Our samples of BNNTs were synthesized by Advanced Materials Laboratory, National Institute for Materials Science (NIMS), Japan. More information about the samples could be obtained from ref. 20–22. BNNTs were dispersed in ethanol using an ultrasonicator, and a few droplets of a suspension containing BNNTs were cast onto a 2000-mesh copper grid. A second 400-mesh copper grid was placed on top of the 2000-mesh grid to sandwich the specimens to enhance their mechanical stability during laser excitation. As a result, the specimen consisted of a woven network of nanotubes with an average thickness of 50 nm. Ultrafast electron diffraction experiments were carried out on our UTEM modified from a JEM-2000EX microscope operated at 160 kV with a LaB₆ cathode (flat area of ~15 μm in diameter). The UTEM was operated either with continuous thermionic electron sources for static structural characterization, or with pulse-laser-excited electron sources for ultrafast pump-probe studies. The probe laser was characterized by a pulse duration of 300 fs, a wavelength of 347 nm and a pulse density of 0.1 μJ per pulse. The pump laser was characterized by a pulse duration of 300 fs, a wavelength of 520 nm, a repetition rate at 200 kHz and variable fluence ranging from 5 to 70 mJ cm⁻². The exposure time for each diffraction pattern was set to 10 seconds. The temporal resolution of the microscope was measured to be about 1 picosecond. More details about the characteristics and the performance of our UTEM have been previously reported in ref. 18 and 19.

Results and discussion

Prior to the ultrafast structural dynamics experiment, we characterized the morphologies and microstructures of BNNTs using conventional TEM techniques. Fig. 1(a) shows the morphologies of the BNNT assembly supported on the Cu-grid. The inset of Fig. 1(a) shows a typical high-resolution lattice image of a single BNNT. In the tubular structure, the normal of (002) planes is along the radial direction and that of (100) planes is along the axial direction. An electron diffraction pattern was taken from a specimen area of about 10 μm in diameter using a selected area aperture, as shown in Fig. 1(b), in which the diffraction rings were indexed using the lattice parameters ($a = 0.250$ nm and $c = 0.666$ nm) of hexagonal boron nitride.⁶ To facilitate structural analysis, the two-dimensional (2D) diffraction pattern was warped and projected into 1D

diffraction profiles, as shown in Fig. 1(c), in which the upper panel shows the as-projected diffraction profiles and the lower panel shows those after background subtraction. Note that the background was fitted with a three-exponential function, and the subsequent analysis of the ultrafast electron diffraction patterns followed the same data process procedure. We also performed an *in situ* TEM heating experiment to determine the lattice expansion coefficients for the BNNTs. Fig. 2(d) shows the measured values of lattice spacing change as a function of temperature. The expansion coefficients for the (002) plane (along the radial direction) and the (100) plane (along the axial direction) were determined to be $3.1 \times 10^{-5} \text{ K}^{-1}$ and $-5 \times 10^{-6} \text{ K}^{-1}$, respectively, which are similar to the measured results for a h-BN crystal.²³ The distinct difference in expansion coefficients for the (100) and (002) planes determined from the static *in situ* heating experiment already points to the fact that BNNTs exhibit a highly anisotropic lattice response to slow thermal heating.

We now discuss the ultrafast electron diffraction measurements performed in a pump-probe setup in our UTEM. Fig. 2(a) shows two typical background-subtracted diffraction profiles that were extracted from the ultrafast diffraction patterns taken at respective time delays of -60 ps and +600 ps for a fluence of 50 mJ cm⁻². An analysis of the changes in diffraction profiles reveals that the positions and intensities of the (002) peak undergo a large change for the two time delays, in sharp contrast to that of the (100) peak. The results show that a large lattice expansion occurs along the radial direction, while lattice changes are very small along the axial direction of BNNTs. The different lattice responses depending on crystallographic orientations clearly suggest highly anisotropic lattice dynamics in BNNTs. Such an anisotropic lattice response from the ultrafast laser excitation experiments is consistent with the results from the slow thermal heating *in situ* experiments. We attribute the anisotropic lattice dynamics to the nature of chemical bonds in the tubular structure of BNNTs, that is, the weak van der Waals bonds between tubular sheets and the strong covalent sp²-hybridized bonds within a tubular sheet. Such an anisotropic behavior of lattice dynamics has been discussed for similar tubular structures of CNTs.^{16–18}

From a structural point of view, the anisotropic dynamic behavior can be well understood based on the characteristics of the chemical bonds of BNNTs. Thermal expansion in solids essentially results from anharmonic oscillations of the constituent atoms. The BNNTs contain weak van der Waals bonds between tubular sheets and strong covalent bonds within a tubular sheet. The covalent bonds are expected to exhibit a fast dynamic response and relatively small lattice expansion, in comparison to the weak van der Waals bonds. The energy potentials for the chemical bonds of BN can be expressed as $U = U(r) + \alpha\delta r^2 + \beta\delta r^3 + \dots$, in which the anharmonic terms are larger for the van der Waals bond than for the covalent bond.¹⁸ Fig. 2(c) shows a schematic representation of the energy potential curves for the intra-sheet and the inter-sheet of the BNNT structure. In particular, the potential for the weak van der Waals bond is highly asymmetric. The average inter-

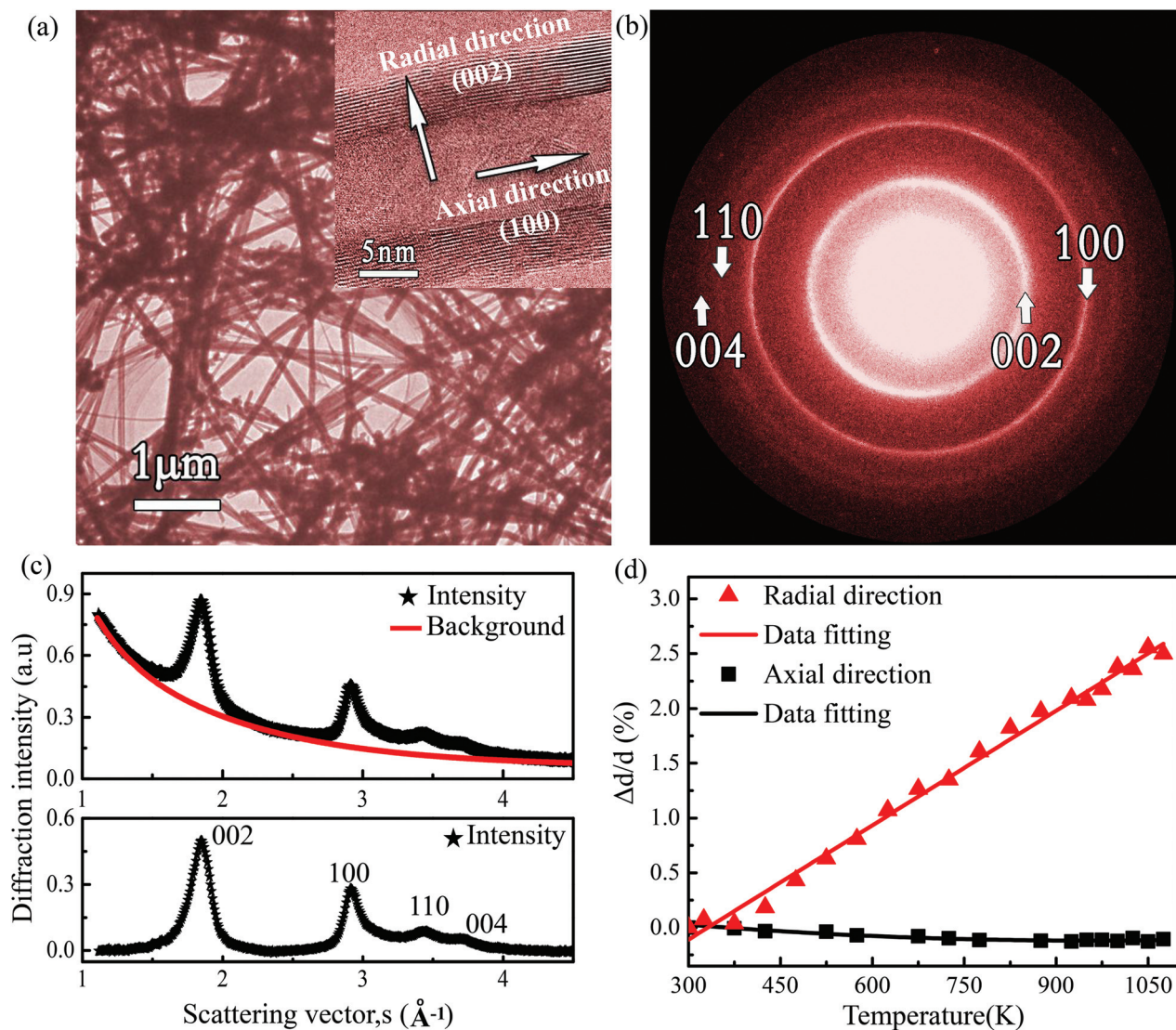


Fig. 1 TEM characterization of multi-walled BNNT samples. (a) TEM image of a BNNT assembly supported on a copper grid and the high-resolution lattice image of a single nanotube. In the tubular structure, the radial direction is along the normal of (002) planes and the axial direction is along the normal of (100) planes. (b) Electron diffraction pattern taken from an area of $10\ \mu\text{m}$ of the BNNT assembly. The Miller indices are indicated using the lattice parameters of hexagonal boron nitride. (c) 1D electron diffraction profiles projected from the 2D electron diffraction pattern. The upper panel is the as-projected diffraction profile (black stars) and the fitted three-exponential function of the background (red curve). The lower panel is the background-subtracted diffraction profile. (d) Lattice expansion coefficients determined from *in situ* TEM heating experiments.

sheet spacing $r_c(T)$ exhibits a considerably large expansion following laser heating owing to the laser excitation of the anharmonic oscillation. It should be noted that the large intersheet thermal expansion observed for the BNNTs is comparable with that of the h-BN interlayer spacing. Since the changes in both lattice position and intensity in the (100) peak are very weak, we now focus on the changes in the (002) peak to characterize the structural evolution of the BNNTs subsequent to laser excitation. Fig. 2(b) shows the changes of the (002) lattice spacing Δd measured from the shifts of the (002) peak position as a function of time delay. An attempt to fit the measured lattice spacing changes with the mono-exponential function yields an unsatisfactory match between the measured

and the fitted data, as seen in Fig. S1 in the ESI.† Instead, a bi-exponential function involving two characteristic time constants can be well fitted to the measurement, as shown in Fig. 2(b), in which $\Delta d(t)/d_0$ is expressed as

$$\begin{aligned} \Delta d(t)/d_0 &= C - \Delta d_{\text{fast}}/d_0 \times \exp(-t/\tau_{\text{fast}}) \\ &\quad - \Delta d_{\text{slow}}/d_0 \times \exp(-t/\tau_{\text{slow}}), \quad (1) \\ C &= \Delta d_{\text{fast}}/d_0 + \Delta d_{\text{slow}}/d_0 \end{aligned}$$

where $\Delta d(t)$ is the change of the (002) lattice spacing at different time delays, d_0 is the lattice spacing prior to laser pulse excitation, Δd_{fast} and Δd_{slow} are the changes of the lattice spacing caused by a fast and a slow process, and τ_{fast}

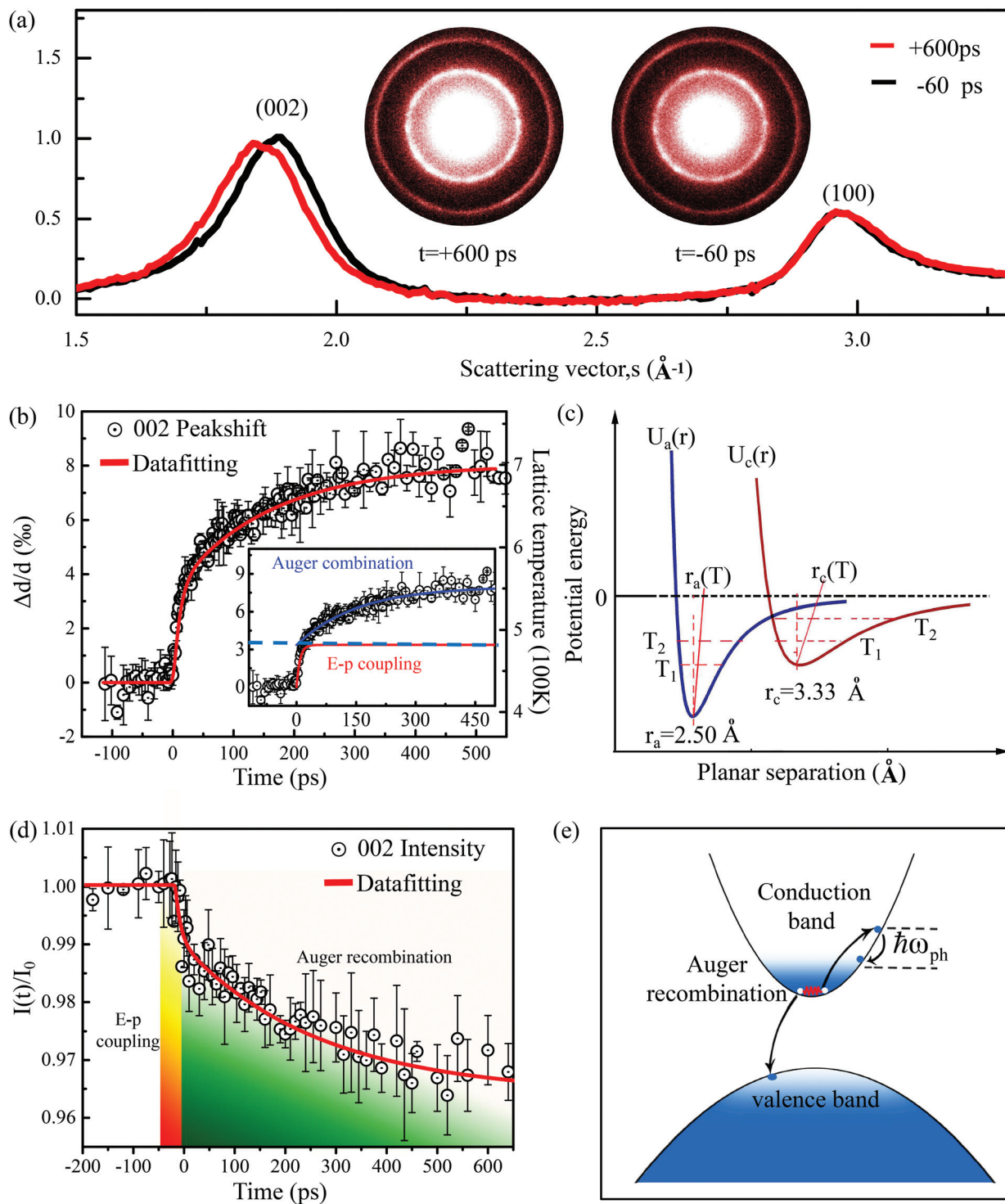


Fig. 2 Ultrafast electron diffraction experiments on multi-walled BNNTs. (a) Two typical diffraction profiles extracted from the diffraction patterns at different time delays of -60 ps and $+600$ ps, showing a large change in the (002) peak position and the intensity while a very small change in the (100) peak for the two time delays. (b) Temporal evolution of the (002) peak positions under a pump fluence of 50 mJ cm^{-2} . The changes in the lattice spacings are fitted with a two-exponential function (red curve). Note that the transient lattice temperatures are estimated by combining the thermal expansion coefficient of 3.1×10^{-5} K^{-1} and the measured changes in the lattice spacings; see text for the detailed calculation. The inset illustrates the bi-exponential function used. (c) Schematics of the energy potential curves of the strong covalent bond in a tubular sheet ($U_a(r)$) and the weak van der Waals inter-sheet bond ($U_c(r)$) along the radial direction. T_1 is the initial temperature and T_2 is the lattice temperature after pumping. (d) Temporal evolution of the (002) peak intensity and the fitting of a two-exponential function to the measured intensity decay. (e) Schematic representation of the Auger recombination process and the secondary phonon emission process.

and τ_{slow} are the respective time constants. The fitting analysis yields the following values: $\tau_{\text{fast}} = 8.5 \pm 1.8$ ps, $\tau_{\text{slow}} = 152 \pm 14$ ps, $\Delta d_{\text{fast}}/d_0 = (3.4 \pm 0.5)\%$, and $\Delta d_{\text{slow}}/d_0 = (4.6 \pm 0.1)\%$. The fast process of lattice dynamics of the BN nanotubes can be attributed to the electron–phonon coupling, by which the photo-excited electron system quickly transfers energy to the phonon system at the nanoscale within a timescale of a few picoseconds. The fast process observed in BNNTs is consistent with that observed in carbon nanotubes, in which strong anharmonic lattice vibrations result in a large inter-sheet motion due to the strong electron–phonon coupling.^{16,18}

While the fast dynamic process can be well understood as being caused by hot electrons thermalizing phonons *via* electron–phonon coupling, identifying the chief cause for the slow dynamic process ($\tau_{\text{slow}} \sim 152$ ps) in the BNNT system requires careful considerations. First, the slow lattice dynamics can be associated with the Auger recombination of electron–hole pairs in the excited states of the BN nanotubes. The electrons in the valence band are excited to the conduction band by three-photon absorption (as discussed below) to generate electron–hole pairs in the excited states.²⁴ The carriers then undergo a series of radiative and nonradiative transitions and contribute to a relatively slow lattice thermalization of BNNTs. Auger recombination, as shown schematically in Fig. 2(e), typically occurs at a time scale of a few 100 ps.²⁵ For example, the Auger recombination process has been identified as a typical secondary thermalization process in the semiconducting GaAs.^{24,26} Moreover, a slow lattice relaxation occurs with time constants ranging from 100 to 300 ps depending on the pump laser fluence, as seen in Fig. S2 in the ESI.† Second, we note that the much slower lattice dynamics can be associated with a delayed emission of transverse-acoustic (TA) phonons up to a nanosecond after laser excitation, as reported for the semiconducting InSb and InP.²⁷ Whether such a slow process with TA phonons can occur in the tubular structures remains an open question. Finally, we consider the heat diffusion and transport between the BNNTs and the Cu grid. The estimated timescale of heat diffusion from the nanotubes to the Cu grids is more than 10 ns estimated by the formula $\tau = \xi^2/4\alpha$, in which τ is the characteristic time of heat diffusion, ξ is the characteristic diffusion length which is larger than the radius of the Cu grid of 4 μm , α is the thermal diffusivity of 220 $\text{mm}^2 \text{s}^{-1}$.²⁸ Alternatively, the thermal heat transport from the Cu grid to the BNNTs can result in a secondary heating of the nanotubes, since strong nonequilibrium conditions can occur between the Cu grid and the BNNTs under an intense pulsed laser. Taking the propagation distance as 4 μm (a typical hole size of ~ 8 μm for a 2000-mesh grid) and the speed of sound in BN being on the order of 15 km s^{-1} ,²⁹ one can estimate the time for acoustic waves to propagate from the Cu grid to the BNNT at the center to be ~ 270 ps. Apparently, this value is somewhat similar to the measured time constants of 100 to 300 ps of the slow process. However, such a value for the heat transport *via* acoustic waves can be regarded as an idealized estimation. In reality, the heat deposited at the Cu surfaces can quickly sink into the interior of Cu grid, and the rough interface between

the Cu grid and the BNNTs can hamper the heat transport by acoustic waves from the Cu grid to the BNNTs. Importantly, the slow process is absent in the ultrafast electron diffraction studies of CNTs with similar diameters (mean diameter of 50 nm), thermal conductivity (300 $\text{W m}^{-1} \text{K}^{-1}$ for CNTs³⁰ and 350 $\text{W m}^{-1} \text{K}^{-1}$ for BNNTs³⁰) and speed of sound along the axial direction, which were also supported on 2000-mesh Cu grids. Thus, the cause of heat diffusion or transport between supporting Cu grid and BNNTs as a secondary heating effect can be discarded.

Using the lattice expansion coefficients (see Fig. 1(d)) determined from the *in situ* TEM heating experiment and the lattice expansions (Fig. 2(b)) following ultrafast laser excitation, the lattice transient temperatures can be calculated by using the formula: $\Delta d(t)/d_0 = \alpha_{002}(T(t) - T_0)$, where $T(t)$ is the lattice temperature for time delay t , and T_0 is the initial temperature. The initial temperature is found to be 430 K, which is above room temperature due to the pumping laser used with a high repetition rate at 200 kHz that results in cumulative heating in the specimen. In the present case, the increases in temperature for the fast and slow processes are measured to be $\Delta T_{\text{fast}} = 110$ K and $\Delta T_{\text{slow}} = 150$ K, respectively.

We now discuss the intensity decay of the (002) peak following laser excitation. Fig. 2(d) shows the normalized intensity of the (002) peak as a function of time delay and the data fitting to a two-exponential function (red curve), yielding the amplitudes of the intensity decrease of about $(1.0 \pm 0.2)\%$ and $(2.7 \pm 0.3)\%$ for the fast and slow components, respectively. The time constant of 8 ± 3 ps for the fast process extracted from the fitting to the intensity decay is similar to the results extracted from the data of lattice changes in Fig. 2(b). The (002) diffraction intensity decay also reflects a fast and a slow process of lattice dynamics, and its interpretation is presented above. The (002) diffraction intensity decay caused by the lattice temperature increase can be expressed as $I(T)/I_0 = \exp(-s^2\delta u^2(T)/3)$, where $I(T)$ is the intensity of a diffraction peak at lattice temperature T , I_0 is the initial intensity, and s is the scattering vector. $\delta u^2(T)$ is the mean-square atomic displacement:³¹

$$\langle \delta u^2(T) \rangle = \frac{9\hbar^2 T}{Mk_B\Theta_D^2} \left(\frac{T}{\Theta_D} \int_0^{T/\Theta_D} \frac{x dx}{e^x - 1} + \frac{\Theta_D}{4T} \right), \quad (2)$$

where the Debye temperature (Θ_D) characterizes the energy scale of thermal motion, \hbar is reduced Planck constant, k_B is the Boltzmann constant and M is the average atomic mass. Using the (002) intensity decay and the estimated temperature rise following laser excitation, we calculated the Debye temperature Θ_D to be about 600 K for inter-sheet thermal vibrations in BNNTs. The calculated Θ_D value is comparable with those of h-BN³² and CNTs.¹⁶

We now turn to the nature of laser absorption in a semiconducting material with a wide band gap. The energy band gap of semiconducting BNNTs ranges from 4 to 6 eV and is independent of the tubular chirality.^{30,33–36} We measured the band gap of the BNNTs used here to be 5.8 ± 0.3 eV by electron energy loss spectroscopy (EELS, data shown in Fig. S3 in the

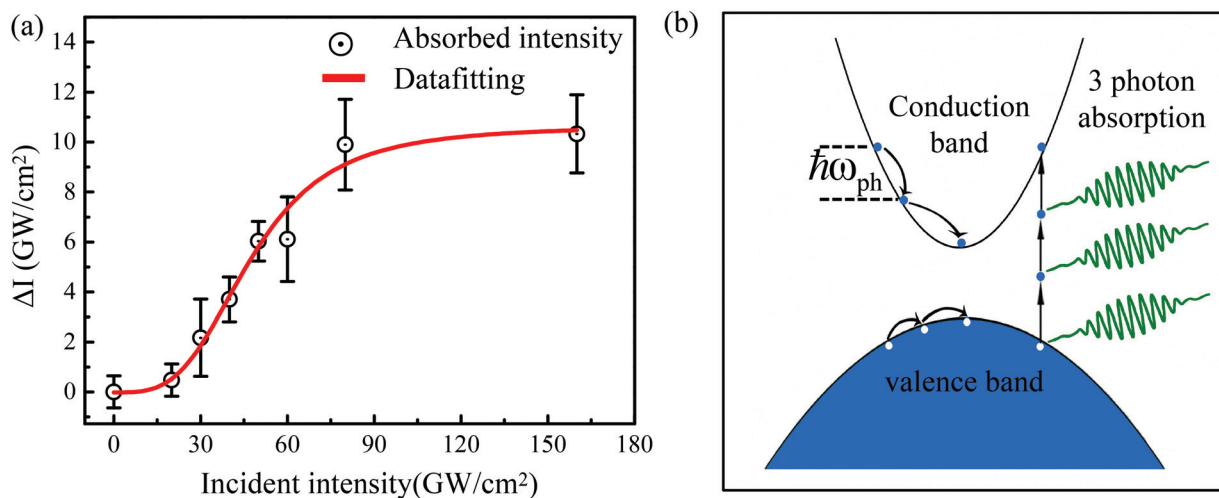


Fig. 3 (a) Absorbed laser intensity (ΔI) as a function of laser input intensity. The measured data are fitted with an equation derived from three-photon absorption (see text for details). (d) The schematic diagram of the three-photon absorption process following the electron–phonon coupling process.

ESI[†]). The photon energy of our pump laser (wavelength 520 nm) is about 2.4 eV; the probabilities of single- or two-photon absorption of the inter-band excitation to occur are extremely low. Considering that the power density used is more than 100 GW cm^{-2} , it is expected that three-photon absorption (3PA) will inevitably occur in the BNNT samples, as shown schematically in Fig. 3(b). The situation has been discussed for other nanoscale systems, *e.g.*, ZnO nanowires³⁷ and h-BN nanofilms.³⁸ We use the 3PA scenario to analyze the nature of the optical absorption in the BNNTs. Fig. 3(a) shows the absorbed laser energy (ΔI) for the BNNTs at different laser fluence values. The ΔI was estimated by using the specific heat capacity of 1.2 J (g K)^{-1} for BN (ref. 39) and the lattice temperature increases at the longest time delay (1 ns) determined from our measurements. The energy dissipation through the Cu supporting grid and thermal irradiation occurred on the time scale of 10 ns and more, which can be neglected. We note that in the present study, a direct measurement of the laser absorption of the BNNTs is difficult because of the porous nature of the BNNT network and the reflection loss caused by the supported TEM grids. The results show that the absorbed laser intensity adopts a power-law relationship in the low-intensity region and becomes saturated in the high-intensity range. In the 3PA process, the intensity change of the incident beam along the propagation direction (z axis) can be described using $dI(z)/dz = -\gamma(I)I(z)^3$, where z and $I(z)$ are the propagation distance and the optical intensity inside the sample, respectively. $\gamma(I)$ is the 3PA coefficient, which nonlinearly changes with the incident laser intensity and becomes saturated at a high laser intensity (the peak power density was about 160 GW cm^{-2} in our experiments). This feature can be described using $\gamma(I) = \gamma_0/(1 + I^3/I_s^3)$, where γ_0 is the 3PA coefficient at the low-intensity approximation, I is the incident laser intensity, and I_s is the saturated incident laser intensity.³⁷ Given that the

propagation distance in the sample is very small, the absorbed laser intensity can be rewritten as $\Delta I = [\gamma_0/(1 + I^3/I_s^3)]I^3\Delta z$, where Δz is the sample thickness of about 50 nm. All of the experimental data in Fig. 3(a) can be well fitted by the above formula, and γ_0 and I_s used in the present fitting curve are $10^{-16} \text{ cm}^3 \text{ W}^{-2}$ and 50 GW cm^{-2} , respectively, which are in good agreement with the results reported for the h-BN film.³⁸

Conclusion

In summary, we have investigated the ultrafast structural dynamics of the BNNTs driven by pulsed femtosecond laser excitation in ultrafast electron diffraction experiments. The time-resolved electron diffraction analysis reveals the highly anisotropic structural dynamics of BNNTs, which can be interpreted in terms of the specific tubular structure and the nature of chemical bonds of BNNTs, *i.e.*, the strong covalent bonds in the intra-sheets and the weak van der Waals bonds in the inter-sheet along the radial direction. Moreover, time-resolved structural analysis yields fast and slow lattice dynamics upon laser excitation. The fast process can be firmly ascribed to the heated electrons thermalizing the phonons *via* strong electron–phonon coupling. The slow process can tentatively be associated with an Auger recombination effect. In addition, a three-photon absorption mechanism and the relevant power-law relationship are discussed for the femtosecond laser excitation of semiconducting materials with large energy band gaps. Our results provide a firm assessment of the characteristics of structural dynamics in BNNTs, and demonstrate the effective use of ultrafast electron diffraction in a transmission electron microscope for exploring the structural dynamics of nanostructured materials.

Conflicts of interest

There are no conflicts to declare.

Acknowledgements

We are grateful to Prof. Xuedong Bai for providing the BNNT samples and the useful discussion. This work was supported by the National Basic Research Program of China 973 Program (No. 2015CB921300), the National Key Research and Development Program of China (Nos. 2016YFA0300300, 2017YFA0504703, and 2017YFA0302900), the Natural Science Foundation of China (Nos. 11604372, 11474323, and 11774391), “Strategic Priority Research Program (B)” of the Chinese Academy of Sciences (No. XDB07020000), and the Scientific Instrument Developing Project of the Chinese Academy of Sciences (No. ZDKYYQ20170002). Z.A.L acknowledges the financial support of the Hundred Talent Program B from CAS.

Notes and references

- 1 Y. Xia, P. Yang, Y. Sun, Y. Wu, B. Mayers, B. Gates, Y. Yin, F. Kim and H. Yan, *Adv. Mater.*, 2003, **15**, 353–389.
- 2 T. Humberto and T. Mauricio, *New J. Phys.*, 2003, **5**, 126.
- 3 S. Iijima, *Nature*, 1991, **354**, 56–58.
- 4 H. Dai, *Acc. Chem. Res.*, 2002, **34**, 1035–1044.
- 5 N. G. Chopra, R. J. Luyken, K. Cherrey, V. H. Crespi, M. L. Cohen, S. G. Louie and A. Zettl, *Science*, 1995, **269**, 966–967.
- 6 D. Golberg, Y. Bando, C. C. Tang and C. Y. Zhi, *Adv. Mater.*, 2007, **19**, 2413–2432.
- 7 B. Hao, A. Asthana, P. K. Hazaveh, P. L. Bergstrom, D. Banyai, M. A. Savaikar, J. A. Jaszczak and Y. K. Yap, *Sci. Rep.*, 2016, **6**, 20293.
- 8 V. Parashar, C. P. Durand, B. Hao, R. G. Amorim, R. Pandey, B. Tiwari, D. Zhang, Y. Liu, A. P. Li and Y. K. Yap, *Sci. Rep.*, 2015, **5**, 12238.
- 9 C. H. Lee, S. Qin, M. A. Savaikar, J. Wang, B. Hao, D. Zhang, D. Banyai, J. A. Jaszczak, K. W. Clark, J. C. Idrobo, A. P. Li and Y. K. Yap, *Adv. Mater.*, 2013, **25**, 4544–4548.
- 10 A. H. Zewail, *Science*, 2010, **328**, 187–193.
- 11 J. S. Kim, T. Lagrange, B. W. Reed, M. L. Taheri, M. R. Armstrong, W. E. King, N. D. Browning and G. H. Campbell, *Science*, 2008, **321**, 1472–1475.
- 12 D. A. Plemmons, P. K. Suri and D. J. Flannigan, *Chem. Mater.*, 2015, **27**, 3178–3192.
- 13 L. Piazza, D. J. Masiel, T. LaGrange, B. W. Reed, B. Barwick and F. Carbone, *Chem. Phys.*, 2013, **423**, 79–84.
- 14 A. Feist, K. E. Echternkamp, J. Schauss, S. V. Yalunin, S. Schafer and C. Ropers, *Nature*, 2015, **521**, 200–203.
- 15 G. M. Vanacore, A. W. P. Fitzpatrick and A. H. Zewail, *Nano Today*, 2016, **11**, 228–249.
- 16 G. M. Vanacore, R. M. van der Veen and A. H. Zewail, *ACS Nano*, 2015, **9**, 1721–1729.
- 17 S. T. Park, D. J. Flannigan and A. H. Zewail, *J. Am. Chem. Soc.*, 2012, **134**, 9146–9149.
- 18 G. Cao, S. Sun, Z. Li, H. Tian, H. Yang and J. Li, *Sci. Rep.*, 2015, **5**, 8404.
- 19 S. Sun, L. Wei, Z. Li, G. Cao, Y. Liu, W. J. Lu, Y. P. Sun, H. Tian, H. Yang and J. Li, *Phys. Rev. B: Condens. Matter*, 2015, **92**, 224303.
- 20 D. Golberg, X. D. Bai, M. Mitome, C. C. Tang, C. Y. Zhi and Y. Bando, *Acta Mater.*, 2007, **55**, 1293–1298.
- 21 C. Zhi, Y. Bando, C. Tan and D. Golberg, *Solid State Commun.*, 2005, **135**, 67–70.
- 22 C. Tang, Y. Bando, T. Sato and K. Kurashima, *Chem. Commun.*, 2002, 1290–1291, DOI: 10.1039/b202177c.
- 23 B. Yates, M. J. Overy and O. Pirgon, *Philos. Mag.*, 2006, **32**, 847–857.
- 24 A. Othonos, *J. Appl. Phys.*, 1998, **83**, 1789.
- 25 S. K. Sundaram and E. Mazur, *Nat. Mater.*, 2002, **1**, 217–224.
- 26 F. Vigliotti, S. Chen, C.-Y. Ruan, V. A. Lobastov and A. H. Zewail, *Angew. Chem., Int. Ed.*, 2004, **43**, 2705–2709.
- 27 M. Trigo, J. Chen, V. H. Vishwanath, Y. M. Sheu, T. Graber, R. Henning and D. A. Reis, *Phys. Rev. B: Condens. Matter*, 2011, **82**, 235205–235209.
- 28 S. Yu, T. Higashihara, M. Tokita, J. Morikawa, J. Watanabe and M. Ueda, *ACS Appl. Mater. Interfaces*, 2013, **5**, 3417.
- 29 Q. Peng, A. R. Zamiri, J. Wei and S. De, *Acta Mech.*, 2012, **223**, 2591–2596.
- 30 J. Wang, C. H. Lee and Y. K. Yap, *Nanoscale*, 2010, **2**, 2028–2034.
- 31 J. J. Gilvarry, *Phys. Rev.*, 1956, **102**, 308–316.
- 32 T. Tohei, A. Kuwabara, F. Oba and I. Tanaka, *Phys. Rev. B: Condens. Matter*, 2006, **73**, 064304.
- 33 H. Chen, Y. Chen, Y. Liu, C.-N. Xu and J. S. Williams, *Opt. Mater.*, 2007, **29**, 1295–1298.
- 34 R. Arenal, O. Stephan, M. Kociak, D. Taverna, A. Loiseau and C. Colliex, *Phys. Rev. Lett.*, 2005, **95**, 127601.
- 35 R. Arenal, O. Stephan, M. Kociak, D. Taverna, A. Loiseau and C. Colliex, *Microsc. Microanal.*, 2008, **14**, 274–282.
- 36 C. H. Lee, M. Xie, V. Kayastha, J. Wang and Y. K. Yap, *Chem. Mater.*, 2010, **22**, 1782–1787.
- 37 B. Gu, J. He, W. Ji and H.-T. Wang, *J. Appl. Phys.*, 2008, **103**, 073105.
- 38 Q. Ouyang, K. Zhang, W. Chen, F. Zhou and W. Ji, *Opt. Lett.*, 2016, **41**, 1368–1371.
- 39 C. Zhi, Y. Bando, C. Tang and D. Golberg, *Solid State Commun.*, 2011, **151**, 183–186.